New Chemical Source of the HCO Radical Following Photoexcitation of Glyoxal, $(HCO)_2$

Robert J. Salter, Mark A. Blitz,* Dwayne E. Heard, Michael J. Pilling, and Paul W. Seakins

School of Chemistry, University of Leeds, Leeds, LS2 9 JT, United Kingdom

Received: April 2, 2009; Revised Manuscript Received: May 23, 2009

Photoexcitation of glyoxal at wavelengths over the range of 395−414 nm was observed to initiate a chemical reaction that produces the HCO radical in addition to the photolytic production of HCO. The technique of dye laser flash photolysis coupled to cavity ring-down spectroscopy was used to determine the time dependence of the HCO radical signal, analysis of which suggests that the chemical source of HCO is the self-reaction of triplet glyoxal

$$(HCO)_2(T_1) + (HCO)_2(T_1) \rightarrow 2HCO + (HCO)_2$$

As the photoexcitation wavelength increases, the production from the triplet glyoxal reaction increases relative to that of HCO from direct photolysis, and at 414 nm, the dominant source of HCO in the system is from the self-reaction of the triplet. The formation of HCO via this process complicates the assignment of the photolysis quantum yield at longer wavelengths and may have been overlooked in some previous glyoxal photolysis studies.

1. Introduction

Glyoxal, $(HCO)_2$, is the smallest α-dicarbonyl and is formed in the troposphere by photooxidation of many volatile organic compounds (VOCs). The OH-initiated oxidations of alkenes,[1] acetylene,[2,3] glycolaldehyde,[4] and aromatics in the presence of NO_x[5−7] have all been identified as sources of glyoxal. These secondary sources, along with primary emissions from combustion (e.g., car exhaust[8,9]), make glyoxal highly relevant for study, especially in the context of urban air pollution and plumes from biomass burning.[10] Elevated concentrations of glyoxal have been measured in urban areas.[11] Most VOCs are removed from the atmosphere by OH-initiated oxidation, however, glyoxal reacts relatively slowly with OH ($k(296\ K) = 8.8 \times 10^{-12}$ cm^3 molecule^{-1} s^{-1}),[12] giving it an atmospheric lifetime with respect to removal by OH equal to ∼24 h.[13] The major removal process for glyoxal in the troposphere is photolysis, with $\tau_{Phot} \approx 2$ to 3 h.[13,14] Photolysis of glyoxal can take place at wavelengths that are readily available within the troposphere, being photolyzed in not only the UV region, where other carbonyl species absorb, but also in the blue region of the visible spectrum, where the atmospheric flux is much greater. Photolysis leads to the production of the formyl radical, HCO, which plays an important atmospheric role as it reacts quickly with O_2 to form HO_2 radicals[15,16]

$$HCO + O_2 \rightarrow CO + HO_2 \qquad (R1)$$

In turn, HO_2 can be converted to OH, for example by reaction with NO, and hence glyoxal photolysis may influence the oxidizing capacity of the atmosphere. Glyoxal may also play a role in the formation of secondary organic aerosol[17−19] affecting surface processes, the Earth's radiative balance, and human health. It is therefore important to have accurate data concerning the rate of removal of glyoxal and production of HCO via its photolysis.

In the region from 250−450 nm the thermodynamically available product channels for the photolysis of glyoxal are[13]

$$(HCO)_2 + h\nu \rightarrow 2HCO \quad \lambda \leq 412\ nm \qquad (P1a)$$

$$\rightarrow HCO + H + CO \quad \lambda \leq 334\ nm \qquad (P1b)$$

$$\rightarrow CH_2O + CO \quad \text{all } \lambda \qquad (P1c)$$

$$\rightarrow H_2 + 2CO \quad \text{all } \lambda \qquad (P1d)$$

$$\rightarrow HCOH + CO \quad \text{all } \lambda \qquad (P1e)$$

$$\rightarrow (HCO)_2(T_1) \qquad (P1f)$$

Photolysis channels P1a and P1b are radical channels, whereas P1c, P1d, and P1e are molecular channels and are thermodynamically open at all wavelengths. P1f is the channel that forms triplet glyoxal, $(HCO)_2(T_1)$, via collision-induced intersystem crossing, and at very long wavelengths, 435 nm, this process results in a near-unity quantum yield for the formation of the triplet at ≤1 Torr total pressure.[20] Integrated over the photolysis wavelengths relevant to the atmosphere, the radical channel P1a is the major channel, but the molecular channel P1c makes a significant contribution.[21]

The complex photochemistry of glyoxal has been investigated extensively. Molecular beam studies have established the existence of P1c and P1d[22−25] at wavelengths, ∼440 nm, beyond the thermodynamic limit for the radical channels. At shorter

* Corresponding author. Fax: +44-0-113-343-6565. E-mail: m.blitz@leeds.ac.uk.

10.1021/jp9030249 CCC: $40.75
Published on Web 07/01/2009

wavelengths, ~395 nm, they have also established that under collision-free conditions HCO radicals may be produced from two different states[26] and have resolved different energy distributions for these two separate pathways.[27] Studies using lamps[21] and laser techniques[28] at higher pressures have gone some way to establishing products under atmospheric conditions, showing that the major product in the atmosphere is the HCO radical. There remains, however, much uncertainty over the actual quantum yields of products,[21,28−30] the mechanism by which they are formed under atmospheric conditions, and the dependence of these processes upon temperature and pressure.

Currently, at Leeds, a comprehensive study on glyoxal photolysis quantum yields as a function of wavelength, pressure, and temperature has just been completed and will be reported in the near future. In the present study, we report on glyoxal photoexcitation at long wavelengths, $\lambda = 395-414$ nm, where the HCO radical is observed to form via a chemical reaction. This newly identified source of HCO is consistent with self-reaction of triplet glyoxal and requires some previous studies of glyoxal to be reappraised.

2. Experimental Section

The technique of laser flash photolysis coupled to cavity ring-down spectroscopy probe was used to photolysis glyoxal and monitor the HCO radical as a function of time. The reaction cell consisted of a jacketed stainless steel tube, where the inner tube had a diameter of ca. 20 mm and the outer jacket had coolant flowing through it to provide temperature control. The flow and temperature of the coolant was controlled using a cryostat (Huber Unistat). At each end of the 60 cm long reaction tube were attached the cavity ring-down mounts, which housed the mirrors (99.98% reflectivity, Layertec). The photoexcitation light was generated from a 532 nm Nd/YAG (Continuum, Powerlite 8010) pumped dye laser (Sirah, PrecisionScan) operating on a DCM/Pyridine1 dye mixture. The output of this dye laser 615−678 nm was mixed with the 1064 nm radiation from the Nd/YAG laser to produce light between 390 and 414 nm. The energy of the photoexcitation light was between 3 and 8 mJ pulse^{-1} and was directed through the reaction cell using right-angle prisms located between the outer jacket and the mirrors. The prisms were located as close to the central axis of the inner tube of the reaction cell as possible without interfering with the cavity ring-down probe beam. This configuration produced a narrow angle of ~1 to 2° between the photoexcitation and probe laser pulses and an axial overlap of 1.2 cm in the double-jacketed region of the reaction cell. The majority of the experiments were carried out at 414 nm, where a constant laser energy of 3.67 mJ pulse^{-1} was used. A solid-state camera (Coherent, Cohu) was used to analyze the dye laser beam profile (Coherent, BeamView Analyzer), for which the cross section was determined to be 0.12 cm^2.

The cavity ring-down probe laser was a Nd/YAG (Spectron SL803) pumped dye laser (Spectron SL4000) tuned to the HCO $A^2A'(0,9,0) \leftarrow X^2A''(0,0,0)$ R bandhead at 613.69 nm, and which typically produced a ring-down time of between 4 and 7 μs. The ring-down signal was detected on a photomultiplier tube and displayed on an oscilloscope (LeCroy, Waverunner LT372), the output from which was transferred via GPIB to a PC for processing between laser pulses. The time delay between the pump and probe laser was controlled by a delay generator (Berkeley Nucleonics Corp. 555).

A typical kinetic trace for HCO consisted of between 100 and 200 points (5 μs per point), with each point the result of averaging between 2 and 6 laser shots. For each time delay point, a background measurement was also made by firing the probe laser before the photolysis laser. At each time point, the ring-down signal was analyzed via fitting a single exponential to the data to determine the decay rate constant, k_{obs}, and the difference between k_{obs} at this time point and the background was used to determine the HCO signal.[31] The lasers were pulsed at 10 Hz.

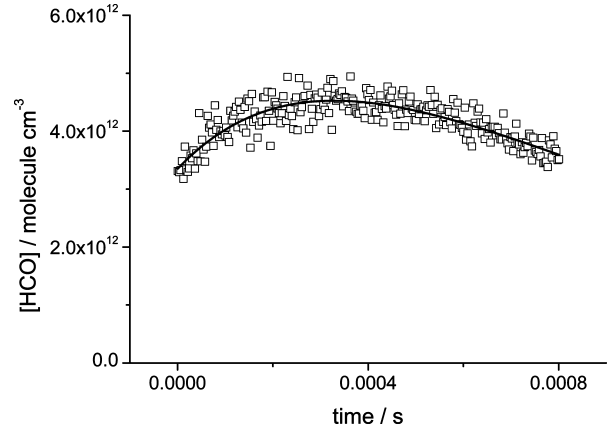

Figure 1. Temporal evolution of [HCO] for [glyoxal] = 1.09×10^{15} molecule cm^{-3} and photoexcited at 404 nm in nitrogen, total density = 1.27×10^{17} molecule cm^{-3}, at 268 K. At time zero, the instant signal is from photolysis and the subsequent growth at longer times is from chemical reaction.

The gases were flowed using mass flow controllers (MKS), with the total flow velocity in the cell such that there was complete sample replenishment every second. The gas pressure was measured close to the reaction cell with a Baratron capacitance manometer (MKS). We produced glyoxal by pyrolyzing glyoxal trimeric dihydrate (Aldrich) in a flowing, inert atmosphere (helium) in the presence of phosphorus pentoxide (P_2O_5) (Aldrich). The gas-phase sample passed through a column of P_2O_5 before being trapped in a Dreschel bottle immersed in liquid nitrogen. The glyoxal purity was checked, and its concentration assigned using a UV/vis spectrometer (Ocean Optics, HR4000). High-purity nitrogen (>99.999%, Air Products) was used straight from the cylinder.

3. Results

The photolysis of glyoxal at wavelengths <395 nm resulted in the instantaneous formation of HCO (reaction P1a), followed by slow removal consistent with diffusion or self-reaction. The slow loss of HCO could be well represented by an exponential decay and is therefore presented as a first-order loss process (e.g., if [HCO] = 1×10^{13} molecule cm^{-3}, then the removal rate is 500 s^{-1}, $k_{HCO+HCO} = 5 \times 10^{-11}$ [32])

$$HCO \rightarrow \text{loss} \qquad \text{(R2)}$$

However, at wavelength ≥395 nmm there was evidence of HCO also forming in a chemical reaction

$$X \rightarrow HCO \qquad \text{(R3)}$$

Figure 1 is an example of this behavior from the photolysis of glyoxal at 404 nm, where the photolytic, time-zero HCO signal is followed by an increase at longer times. At 404 nm, the yield of HCO formed from photolysis is larger than that from HCO formed from chemical reaction. However, as the wavelength was increased, the amount of HCO formed from

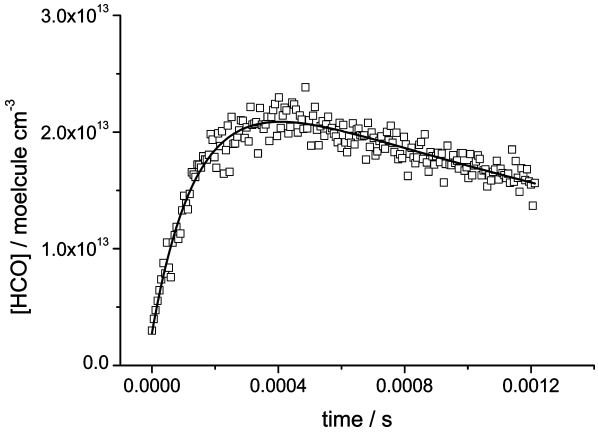

Figure 2. Temporal evolution of [HCO] for [glyoxal] = 10.6×10^{15} molecules cm^{-3} and photoexcited at 414 nm in nitrogen, total density = 1.93×10^{18} molecules cm^{-3}, at 233 K (experiment 22k, Table 1). At time zero, the instant signal is from photolysis, and the subsequent growth at longer times is from reaction R4.

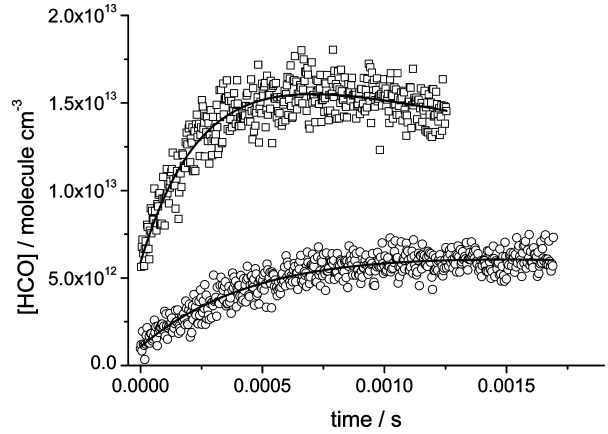

Figure 3. Temporal evolution of [HCO] for [glyoxal] = 2.74×10^{15} molecule cm^{-3} and photoexcited at 409 nm in nitrogen, total density = 2.78×10^{18} molecule cm^{-3}, at 233 K. The two traces correspond to low (1.7 mJ/pulse, ○) and high (5 mJ/pulse, □) laser pulse energies. At time zero, the instant signals from photolysis are proportional to the excitation pulse energies and the growth rate and amount of HCO from reaction R4 also scales with laser excitation pulse energy.

this unknown reaction, R3, became the dominant source of HCO in the system. Figure 2 shows an example of this behavior from the photolysis of glyoxal at 414 nm. This kinetic trace shows a small amount of photolytic HCO, formed at time zero via channel P1a, and then at longer times, HCO is formed via a chemical reaction, R3. The analytical solution to this kinetic scheme, P1, R3, and R2 is given by the equation

$$[\mathrm{HCO}] = \frac{[\mathrm{X}]_0 k_{\mathrm{R3}}}{k_{\mathrm{R3}} - k_{\mathrm{R2}}}[\exp(-k_{\mathrm{R2}}t) - \exp(-k_{\mathrm{R3}}t)] + [\mathrm{HCO}]_0 \exp(-k_{\mathrm{R2}}t) \quad \text{(E1)}$$

where $[HCO]_0$ is the instantaneously produced photolytic HCO from P1a, $[X]_0$ is the unknown source that produces HCO with a rate constant k_{R3}, and k_{R2} is the rate constant for the slow loss of HCO in the system, which is reasonably approximated by a single exponential loss function. Equation E1 was fitted to the experimental data, as shown in Figure 2. However, when the laser photolysis energy was varied, it was observed that the HCO growth rate constant, k_{R3}, changed dramatically. Figure 3 shows the effect of changing the laser energy from 1.7 to 5 mJ/pulse. This observation would appear to rule out the possibility that reaction R3 is (pseudo) first-order and strongly suggests that it is second-order in a photolytically generated species. It is proposed that this second-order reaction is the self-reaction of triplet glyoxal

$$(\mathrm{HCO})_2(\mathrm{T}_1) + (\mathrm{HCO})_2(\mathrm{T}_1) \rightarrow 2\mathrm{HCO} + (\mathrm{HCO})_2(\mathrm{S}_0) \quad \text{(R4)}$$

This proposed reaction is consistent with the results of the detailed glyoxal photochemical study presented elsewhere[33] that demonstrates that a continuously increasing triplet population is created as the wavelength is increased beyond 395 nm. The formation of triplet glyoxal at long wavelengths is wholly consistent with the study by Anderson et al.[20] in which a near unity triplet yield was observed at a photoexcitation wavelength of 435 nm and a total pressure ~1 Torr for channel P1f. This formation of triplet glyoxal at long wavelengths is the basis of a new field instrument that determines glyoxal concentration via phosphorescence from the photoexcited triplet.[34] In addition, analogous triplet population behavior has previously been observed in the photochemistry of acetone.[35]

Triplet glyoxal formed at these long wavelengths does not have sufficient energy to dissociate to HCO, but the combined energy from self-reaction is sufficient to promote the dissociation of one triplet molecule to 2HCO. When reaction R4, rather than R3, is used to describe the chemical production of HCO and a numerical integration fitting program (FACSIMILE) is used,[36] only a minimal improvement in the fit to the data in Figures 1 and 2 was found compared with using eq E1. Initially, this was surprising because describing the HCO chemical production via second-order kinetics is expected to show distinctly different results than production from first-order kinetics. But the present coupled growth and loss kinetics are such that the growth kinetics are observed over not much more than one or two half lives. This effect results in the lack of distinction between first- and second-order growth kinetics.

The laser energy dependence of the HCO signal, as in Figure 3, can be used to distinguish between possible chemical sources of HCO. All data collected at 414 nm were analyzed using the mechanism containing the processes P1a, P1f, R2, and R4. The analysis of the HCO temporal profile with this mechanism was obtained via numerical integration (FACSIMILE)[36] because there is no simple analytical solution and the kinetic parameters k_4, k_2, [HCO](P1a), and [$(HCO)_2(T_1)$](P1f) were adjusted to best fit the data, as shown in Figures 2 and 3. In this analysis, the initial concentration of excited glyoxal via P1a + P1f = P1 was fixed to the estimate given by the product of the glyoxal concentration, the glyoxal absorption cross section at 414 nm, 1.01×10^{-19} cm^2,[21] and the laser fluence of 6.1×10^{16} photon cm^{-2}, derived using the photolysis laser beam cross section of 0.12 cm^2 determined from a beam profiler. These experiments at 414 nm were completed in two days with only minimal adjustment of the alignment of the CRDS probe laser for HCO detection and hence support the assumption that the overlap of the photolysis and probe beams was constant. The results of the above analysis for experiments over a range of temperatures and total pressure (in N_2) are given in Table 1 and are summarized in Table 2.

4. Discussion

The formation of the excited singlet state, S_1, of glyoxal via laser excitation is instant on the time scale of these experiments.

TABLE 1: Values of k_{R4} and Yields of HCO from Photolysis of Glyoxal and from Chemical Source Following Photoexcitation at 414 nm under Different Experimental Conditions

expt	*T*/K	10^{-18} [N_2]/ molecule cm^{-3}	10^{-14} [glyoxal]/ molecule cm^{-3}	10^{11} k_{R4}/cm^3 molecule^{-1} s^{-1}	10^{-11} [HCO]$_0$/ molecule cm^{-3}	[(HCO)$_2$(T_1)]$_0$/ [HCO]$_0$
23h	298	6.86	6.33	15 ± 10	2.1 ± 1.2	10.4
23j	298	6.92	12.7	9.2 ± 7.8	4.8 ± 3.7	9.2
23l	298	6.91	25.3	10.0 ± 8.9	8.0 ± 7.0	11.0
23n	298	6.85	37.7	10.5 ± 9.4	9.2 ± 6.6	14.2
23m	298	6.87	74.7	11 ± 10.	24 ± 18	10.9
23k	298	6.86	86.6	12 ± 11	24 ± 28	12.5
23i	298	6.86	99.0	10.5 ± 9.3	32 ± 23	10.7
23a	298	1.91	7.2	7.0 ± 4.7	4.2 ± 2.9	8.7
23c	298	1.93	14.3	4.2 ± 3.6	12 ± 11	5.8
23e	298	1.93	28.5	4.8 ± 4.4	19 ± 17	7.4
23g	298	1.91	55.1	4.5 ± 4.2	34 ± 30	7.1
23f	298	1.93	81.7	4.6 ± 4.2	45 ± 38	9.2
23d	298	1.91	93.3	4.6 ± 4.3	58 ± 50	8.1
23b	298	1.94	107	5.1 ± 4.7	56 ± 50	9.6
22j	233	1.94	28.7	2.6 ± 2.5	6.0 ± 4.4	26.7
22l	233	1.93	41.8	2.5 ± 2.3	9.5 ± 7.4	24.3
22n	233	1.92	55.3	2.2 ± 2.1	10.0 ± 6.9	30.6
22o	233	1.95	82.2	1.8 ± 1.7	19 ± 15	23.6
22m	233	1.94	94.6	1.8 ± 1.7	26 ± 20	20.0
22k	233	1.93	106	1.7 ± 1.6	46 ± 40	12.7
22c	343	1.93	7.2	5.2 ± 3.2	12 ± 11	2.51
22a	343	1.92	14.4	6.9 ± 5.8	21 ± 20	2.90
22e	343	1.92	28.3	6.7 ± 6.1	36 ± 34	3.31
22g	343	1.90	41.2	6.6 ± 6.0	53 ± 50	3.31
22i	343	1.92	55.4	7.6 ± 6.9	64 ± 58	3.70
22h	343	1.93	68.7	7.5 ± 6.7	78 ± 70	3.75
22f	343	1.92	81.1	7.5 ± 6.7	89 ± 80	3.88
22d	343	1.97	95.8	7.7 ± 7.6	106 ± 96	3.77
22b	343	1.90	104	6.6 ± 6.1	130 ± 130	3.3

TABLE 2: Weighted Average of Some Values in Table 1 Following Glyoxal Photoexcitation at 414 nm

T/K	10^{-18} [N_2]/ molecule cm^{-3}	10^{11} k_{R4}/cm^3 molecule^{-1} s^{-1}	[(HCO)$_2$(T_1)]$_0$/ [HCO]$_0$
298	6.87	10.8 ± 3.1	11.3 ± 1.6
298	1.92	4.9 ± 1.6	7.7 ± 2.5
233	1.94	2.0 ± 0.8	20.2 ± 6.6
343	1.92	6.4 ± 1.9	3.3 ± 1.0

Intersystem crossing from S_1 to the triplet state, T_1, is rapid (submicrosecond time scale) and shorter than the time resolution of the temporal profiles of HCO shown in Figures 2 and 3. Therefore, the triplet can be considered to be formed instantaneously and given an initial value in the numerical integration. Figure 2 implies that there is a chemical source of HCO in the system, and Figure 3 shows that the observed HCO kinetics are dependent on the laser photoexcitation energy. The simplest explanation of the results exemplified in Figures 1, 2, and 3 is that the chemical formation of HCO in the system is consistent with triplet glyoxal self-reaction R4. This conclusion is quantified by our data analysis, which is summarized in Tables 1 and 2. From Table 1, it is observed that a consistent value for the self-reaction of triplet glyoxal, k_{R4}, is returned over a wide range of glyoxal concentrations at a given temperature.

Figure 4 shows an example of individually returned values for k_{R4} from fits to the experimental data at different glyoxal concentrations. The initial triplet concentration will scale with glyoxal concentration. The uncertainty in the determination of k_{R4} is large, which is to be expected because several parameters are varied during the best-fit procedure. Within the uncertainty, there is no systematic change in k_{R4} with glyoxal concentration. The uncertainties in k_{R4} given in Table 2 are the weighted averages from all values of k_{R4} in Table 1, which were determined over a range of glyoxal concentrations (typically 7×10^{14} to 1×10^{16} molecule cm^{-3}). The actual errors will be larger because of the errors due to the measurement of flow rate and pressure and, more importantly, the errors in the determination of the initial concentration of photoexcited glyoxal. (See above.)

The thermodynamics for HCO formation from glyoxal photolysis show that beyond 412 nm, HCO can be formed only by excitation via hot bands.[37] Therefore, the stabilized triplet state formed from long wavelength photoexcitation of glyoxal does not have enough energy to dissociate directly to HCO. However, the two triplet states together do have sufficient energy to bring about dissociation via reaction R4 by energy pooling. If reaction R4 produced only one HCO radical, then the k_{R4} values in Table 1 would be approximately doubled. Although

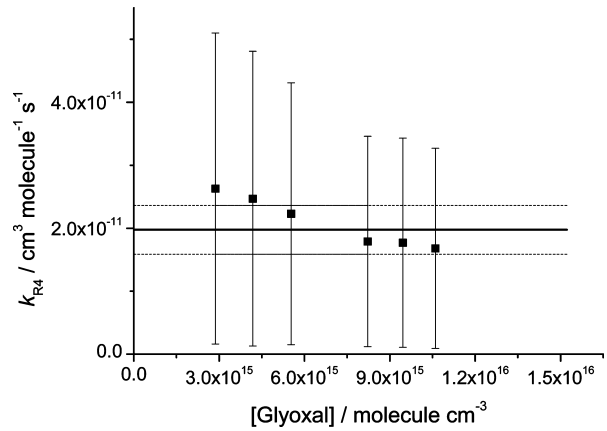

Figure 4. Returned rate coefficients for reaction R4, k_{R4}, from analyzing the 414 nm, 233 K data using the mechanism P1a, P1f, R4, and R2. The bold line is the weighted average of k_{R4} and is equal to 1.97×10^{-11} cm^3 molecule^{-1} s^{-1}, and the dashed lines are the confidence limits.

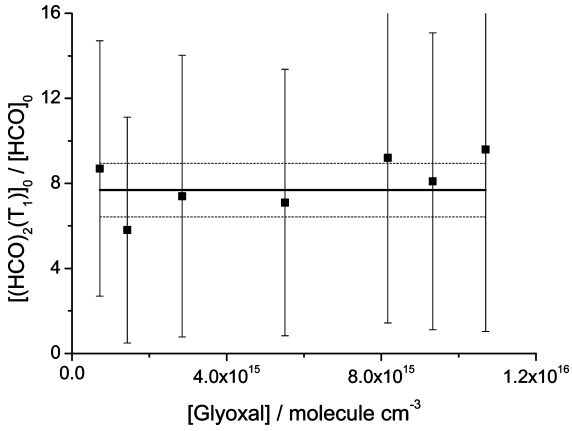

Figure 5. Ratio $[(HCO)_2(T_1)]_0/[HCO]_0$ obtained from the kinetics traces at 298 K at total density $[N_2] = 1.92 \times 10^{18}$ molecule cm^{-3} (experiments 23a−g). The average of this ratio is equal to 7.7 (the dashed lines are the confidence limits) and appears to be independent of glyoxal concentration.

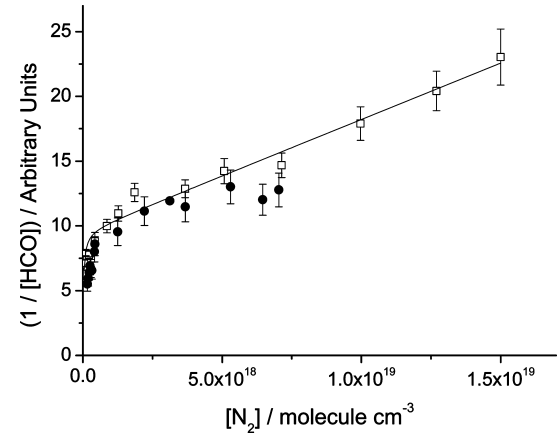

Figure 6. Stern−Volmer plot of the reciprocal yield of HCO versus total N_2 density obtained following the photolysis of glyoxal at 414 nm and 298 K. □ and ● are data obtained on separate occasions, and whereas both sets are consistent, within error, the returned triplet glyoxal yields are significantly different, especially at high pressure. The solid line is the best fit to the □ data and is used to calculate the parameters in Table 3. These data are taken from our forthcoming paper on glyoxal photolysis.

the production of HCO via reaction R4, a process not previously reported in the literature, is wholly consistent with the experimental data, a more complicated mechanism cannot be ruled out, but the formation of HCO must involve triplet glyoxal.

In the kinetic analysis, the HCO absorption signal is converted to absolute concentration using an estimated laser photolysis/probe path length overlap of 1.2 cm and an HCO absorption cross section of $\sigma_{HCO,613.69nm} = 1.6 \times 10^{-18}$ cm^2.[38] The path length is consistent with the geometry of the laser beams and was calculated using the HCO yields from our glyoxal photolysis experiments. (See below.) There is a considerable range of values for $\sigma_{HCO,613.69nm}$ in the literature, $(\sim 1.6-3.6) \times 10^{-18}$ cm^2.[39] The value chosen here is at the low end of the range but was determined using excimer laser photolysis to generate the HCO radical.[38] An excimer laser produces a more even photon flux compared with dye lasers and hence should provide a more reliable estimate of $\sigma_{HCO,613.69nm}$. The beam profiler showed that the profile of our dye laser had a large intensity gradient across the beam, with the intensity at the center being three times the average. This type of beam profile is common to dye lasers and is the main source of uncertainty in the accuracy of our k_{R4} determination. The dye laser photolysis beam and the probe CRDS laser beam were overlapped to maximize the HCO signal. Overall, the uncertainty in k_{R4} could readily be a factor of two or three. The errors in Table 2 reflect the precision in the measurements, not the accuracy. However, the purpose of this article is not to determine an accurate value of k_{R4} but rather to highlight the formation of HCO from a chemical source following the excitation of glyoxal, to postulate the origin of this HCO, and to stress the importance of taking it into account in the determination of HCO photolysis quantum yields from glyoxal photolysis in laboratory experiments.

Tables 1 and 2 also give the ratio of the initial triplet glyoxal to initial HCO concentrations, $[(HCO)_2(T_1)]_0/[HCO]_0$ where $[(HCO)_2(T_1)]_0$ and $[HCO]_0$ were floated parameters in the data analysis but $[(HCO)_2(T_1)]_0 + [HCO]_0$ was fixed to the initial amount of photoexcited glyoxal. (See above.) Table 1 shows that this ratio is independent of glyoxal concentration, as shown in Figure 5. Table 2 gives the weighted average. Again, as previously stated for k_{R4}, these errors shown for the ratio at different temperatures and pressures relate to the precision of the measurements. In addition, if the proposed mechanism for HCO formation is correct, then this $[(HCO)_2(T_1)]_0/[HCO]_0$ ratio may be compared to $[(HCO)_2(T_1)]_0/[HCO]_0$ independently obtained from our glyoxal photolysis HCO quantum yield measurements. How our glyoxal photolysis HCO quantum yield measurements yield $[(HCO)_2(T_1)]_0/[HCO]_0$ will be fully detailed in our forthcoming publication[33] and is only outlined here. An example of data for the HCO photodissociation quantum yield from glyoxal is shown in Figure 6 for 414 nm and 298 K. The data are shown as a Stern−Volmer plot of the reciprocal of the instantaneously formed HCO from channel P1a plotted versus number density of the buffer gas, N_2. The HCO signal does not include any contribution from reaction R4 because it is obtained at zero time delay. The Stern−Volmer plot is curved and is characterized by two pressure regimes: a low-pressure regime with a large gradient and a high-pressure region with a small gradient. This type of behavior was previously observed in the determination of CH_3CO yields following the photolysis of acetone at longer wavelengths[35] and was interpreted in terms of dissociation via two different electronically excited states of acetone. At high pressure, dissociation is mainly from the initially prepared singlet S_1 state, whereas at low pressure, dissociation from the triplet T_1 state is dominant, with population of T_1 via intersystem crossing from S_1. The slope of the Stern−Volmer plot represents the ratio of the rate of dissociation compared with that of collisional quenching from the dissociating state. Full details of this two-state mechanism and its interpretation can be found in our previous paper on acetone photolysis,[35] but for the present article, the high-pressure approximation is utilized.

From Figure 6, the Stern−Volmer (SV) plot is in the high-pressure linear regime above a pressure of 10^{18} molecule cm^{-3}, and in this regime, the SV is given by

$$SV_{HCO,P1a} = (1 + INT_{HP} + k_{S1,quench}[M])/2 \quad (E2)$$

where $SV_{HCO,P1a}$ is the reciprocal pressure-dependent yield of HCO from the photolysis of glyoxal, $(1 + INT_{HP})$ is the high-pressure intercept, $k_{S1,quench}$ is the Stern−Volmer quenching parameter, and the factor of 2 accounts for the HCO photolysis yield from glyoxal channel P1a being two. INT_{HP} is related to the quenched thermally stable triplet glyoxal, which is given by

$$(HCO)_2(T_1)_{yield} = \frac{(INT_{HP})/2}{SV_{HCO,P1a}} \quad \text{(E3)}$$

where $(HCO)_2(T_1)_{yield}$ is the triplet glyoxal yield. At high pressures, all of the triplet state is stabilized below the dissociation threshold. In addition, stabilization of S_1 also occurs, further reducing the yield of two. The intercept obtained by extrapolation of the high-pressure section of the SV plot corrects for this further reduction in HCO and gives the yield of the triplet state, resulting in eq E3.

Because $SV_{HCO,P1a}$ is the Stern−Volmer value of the HCO yield, it follows that at the high-pressure intercept

$$(HCO)_2(T_1)_{yield}/HCO_{yield} = (INT_{HP})/2 \quad \text{(E4)}$$

where HCO_{yield} is the total HCO from glyoxal photolysis. The values for $SV_{HCO,P1a}$, $(HCO)_2(T_1)_{yield}$, and $(HCO)_2(T_1)_{yield}/HCO_{yield}$ are given in Table 3 for the pressures and temperatures of the experiments. In the last column of Table 3, the ratios of $(HCO)_2(T_1)_{yield}/HCO_{yield}$ from Tables 2 and 3 are given, where the values from Tables 2 and 3 are subscripted reaction and SV, respectively. The agreement between these two methods for obtaining $[(HCO)_2(T_1)]_0/[HCO]_0$, one method using the Stern−Volmer analysis of the instantaneous photolytic HCO signal and one using the entire HCO temporal profile that includes both instantaneous and delayed chemical production of HCO, is reasonably good taking into account the combined errors of both methods. This comparison supports the hypothesis that reaction R4 is responsible for the delayed chemical production of HCO in the system.

Table 3 shows that for photoexcitation at 414 nm, there is a significant population of the triplet, $(HCO)_2(T_1)_{yield}$, with the yield following excitation being >0.5. The assignment of this yield is derived using a Stern−Volmer analysis of the data assuming the acetone-like[35] photolysis mechanism described above. However, in the literature,[26] there is an alternative photodissociation mechanism described for glyoxal in which the high-pressure regime of the Stern−Volmer plot (Figure 6) results from the formation of HCO following dissociation of the ground electronic state, S_0, of glyoxal, formed after internal conversion from the initially excited S_1 state. This alternative mechanism predicts an even larger yield of triplet glyoxal of >0.8 for all conditions given in Tables 1 and 2, and using this mechanism, the value of k_{R4} is smaller, whereas the ratio $(HCO)_2(T_1)_{yield}/HCO_{yield}$ is larger. The returned values will be changed by no more than a factor of two from those given in Tables 1 and 2. The reason why we favor the acetone-like mechanism will be fully discussed in our forthcoming publication on glyoxal photolysis.

Whereas we have already noted the significant error in the parameters given in Table 2, there do appear to be trends that require further comment. At 298 K, k_{R4} doubles as the density of N_2 is increased from (1.9 to 6.9) $\times 10^{18}$ molecule cm^{-3}, but if reaction R4 occurs via energy transfer, which seems most likely, and is consistent with the temperature dependence observed for k_{R4}, then the observed increase in k_{R4} with pressure is most likely anomalous. The source of this anomaly is probably associated with the assigned $(HCO)_2(T_1)_{yield}$ that was used in the data analysis. In the analysis of the high pressure 298 K data, the $(HCO)_2(T_1)_{yield}$ was calculated using the 0.59 yield of triplet given in Table 3, but if this yield was 0.75, then the returned k_{R4} is halved. This dramatic reduction in k_{R4} is a consequence of reaction R4 being a second-order reaction and hence having a squared dependence on $(HCO)_2(T_1)_{yield}$. The assigned 298 K $(HCO)_2(T_1)_{yield}$ yields in Table 3 were obtained from fitting data indicated by open squares in Figure 6. The data indicated by filled circles in Figure 6 were obtained on a different day, and whereas, within the errors, they are consistent with the black, open squares, fitting to the latter (filled circles) data gives a triplet yield, $(HCO)_2(T_1)_{yield}$, > 0.8 at the higher pressure. The high value for k_{R4} in Table 2 may therefore be anomalous and is a consequence of its sensitivity to the assigned T_1 yield. However, this sensitivity becomes dramatically lessened as the T_1 yield approaches 1.0. Therefore, on this basis, the other k_{R4} values in Table 2 are expected to be better defined. If just the lower-pressure data are considered, then it does appear that k_{R4} significantly increases with temperature, which is consistent with reaction R4 not being an association reaction on a barrierless surface. The consistency of the $(HCO)_2(T_1)_{yield}/HCO_{yield}$ values in Tables 2 and 3 for a range of glyoxal concentrations at a given temperature supports R4 as the source of the chemically produced HCO in the system, and variability in this ratio can be readily assigned to the uncertainty in the T_1 yield, but unlike k_{R4}, $[(HCO)_2(T_1)]_0/[HCO]_0$ values in Table 2 scale linearly with the assigned T_1 yield.

Reaction R4 has important consequences for the interpretation of HCO yields from studies on glyoxal photolysis. At wavelengths greater than 380 nm, glyoxal photolysis exclusively produces formyl radicals

$$(HCO)_2 \rightarrow 2HCO \quad \text{(P1a)}$$

with the HCO quantum yield being pressure-dependent via quenching of the relatively long-lived excited state of glyoxal.[28] However, in our study on glyoxal photolysis, which will be reported in the near future,[33] at wavelengths ≥395 nm, intersystem crossing starts to populate the triplet state of glyoxal, $(HCO)_2(T_1)$, via channel P1f. In this study, by using 414 nm light to photolyze glyoxal, it is possible to distinguish the instant photolytic HCO (P1a) from the time-dependent HCO from reaction R4 by following the temporal profile of the HCO signal (Figures 2 and 3) and quantify the contributions of each to the HCO at any time by fitting to the kinetic scheme on the basis of the processes, P1a, P1f, R4, and R2.

However, in the study by Zhu et al.,[28] the temporal profile of HCO was not measured, rather the time delay between the photoexcitation laser and the HCO CRDS probe laser was fixed,

TABLE 3: Yield of Triplet State of Glyoxal, Parameters from a Stern−Volmer Analysis of the HCO Quantum Yield Following Photoexcitation at 414 nm under a Variety of Conditions

T/K	10^{-18} $[N_2]$/molecule cm^{-3}	$(HCO)_2(T_1)_0$	$SV_{HCO,P1}$	INT_{HP}	$((HCO)_2(T_1)_0/HCO_0)_{SV}$	$ratio_{SV}/ratio_{reaction}$[a]
298	6.87	0.59	15.5	18.1	9.1	0.8
298	1.92	0.82	11.1	18.1	9.1	1.2
233	1.94	0.96	15.3	29.4	14.7	0.7
343	1.92	0.83	7.8	12.9	6.5	0.5

[a] $Ratio_{SV} = \{(HCO)_2(T_1)_0/HCO_0\}_{SV}$ values from Table 3 and $ratio_{reaction} = [(HCO)_2(T_1)]_0/[HCO]_0 =$ values from Table 2.

and it was assumed that all observed HCO signals originated solely from photolysis with no allowance made for any other source of HCO at longer time, for example via R4. This means that at the wavelengths where the thermalized triplet state is populated, the HCO quantum yields following glyoxal photolysis reported by Zhu et al. are potentially overestimated. This overestimation becomes greater at longer wavelengths, where the HCO photolysis yields decrease (because of the larger impact of collisional quenching of longer-lived glyoxal excited states) but the T_1 populations (and hence the impact of reaction R4 as a source of HCO) increase. For example, Zhu et al. monitored HCO using CRDS at a fixed time of 15 μs using typically $[(HCO)_2] = 10^{17}$ molecule cm^{-3}, which is 10 times greater than the concentrations used in this study. Whereas the dye laser energies were not quoted for individual wavelengths, it is reasonable to assume that the laser fluences between 380 and 420 nm were at least as large as those used in this study if their quoted dye laser system was operating at manufacturer's specification. Under these conditions, Zhu et al. would have observed a rate of HCO formation from reaction R4 that is at least ten times faster than that seen in Figure 2, where the concentration is 10 times less, $[(HCO)_2] \approx 10^{16}$ molecule cm^{-3}. The half-life for HCO formation in Figure 2 is $\sim$100 μs; therefore, under the conditions used by Zhu et al.,[28] it is most likely that at a fixed delay time of 15 μs, reaction R4 would be close to completion and the dominant source of HCO at that time, with only a minor contribution from the photolysis channel P1a, which is the reported quantity. This effect has been quantified by comparing the HCO quantum yields from Zhu et al. to those obtained in this study. From Figure 6, a modest extrapolation of the Stern−Volmer plot at 414 nm and 298 K to 760 Torr (2.5×10^{19} molecule cm^{-3}) predicts an HCO quantum yield of $\sim$0.03. The corresponding value from the data of Zhu et al. is $\sim$0.2, implying that the majority of the HCO signal at this wavelength in the Zhu study was from reaction R4 and not from glyoxal photolysis (channel P1a). It may be prudent to reassess the data from Zhu et al. at wavelengths $\geq$395 nm to take into account reaction R4 as a source of HCO.

Tadic et al.[21] studied glyoxal photolysis using continuous steady-state photolysis by a range of UV/visible lamps; a range of detection methods was used to identify the end products. In their study, air was used as the buffer gas, which is not possible in the current study because of the rapid reaction R1. Therefore, in the presence of large excess of O_2, it is reasonable to expect the triplet glyoxal, $(HCO)_2(T_1)$, to be rapidly quenched

$$(HCO)_2(T_1) + O_2 \rightarrow ? \qquad \text{(R5)}$$

because triplet−triplet reactions are spin-allowed processes. For experiments performed in air, there is therefore little chance of any $(HCO)_2(T_1)$ reacting via R4, and it might be expected that the study of Tadic et al. is not subject to this potential interference and was better able to assign the HCO photolysis quantum yields. This appears to be the case as Tadic et al.[21] report the HCO yield at 415 nm and 760 Torr to be 0.016, which is comparable to our value of $\sim$0.03 obtained at 414 nm from extrapolation of Figure 6. It should be stressed that under atmospheric conditions, because of the presence of O_2, reaction R4 is not expected to play any significant role in the formation of HCO following photoexcitation of glyoxal at longer wavelengths.

While the present study and that of Tadic et al. appear to be in fair agreement at 415 nm, it is noted that at 380 nm, Tadic et al. report $\Phi_{HCO}(760\ \text{Torr}) = 0.21$, which is less than half that of the value of 0.49 reported by Zhu et al.[28] At 380 nm, we have determined that the triplet is not populated, and our Φ_{HCO} result is in good agreement with that of Zhu et al.[28] Therefore, whereas the integrated glyoxal photolysis quantum yields of Tadic et al. correspond to their results from broadband lamp photolysis, the photolysis quantum yields at an individual wavelength may vary considerably. Our future publication on glyoxal photolysis will provide an accurate direct determination of HCO quantum yield as a function of pressure, wavelength, and temperature, and when parametrized appropriately, provide accurate photolysis quantum yields for atmospheric modeling.

5. Conclusions

The present study has identified a new chemical source of the HCO radical following the photoexcitation of glyoxal at wavelengths $\geq$395 nm. This chemical source results in a growth after photoexcitation at time zero of the HCO radical, and the magnitude of the growth, compared with the HCO produced at time zero from photolysis, is observed to increase with increasing wavelength. This amount of chemically produced HCO tracks the population of the triplet glyoxal, $(HCO)_2(T_1)$, formed following photoexcitation of glyoxal and which has been characterized fully in a separate study on glyoxal photolysis.[33] In addition, the HCO growth rate and the amount of chemically produced HCO were observed to scale with laser excitation energy. From these observations, we propose that the HCO radical source reaction is

$$(HCO)_2(T_1) + (HCO)_2(T_1) \rightarrow 2HCO + (HCO)_2 \qquad \text{(R4-1)}$$

By analyzing the temporal evolution of HCO at 414 nm, we have quantified the occurrence of reaction R4, measured the rate constant for this reaction, k_{R4}, and determined the ratio of the triplet glyoxal concentration to the instantaneously generated photolytic yield of HCO, $[(HCO)_2(T_1)]_0/[HCO]_0$. This ratio was independently obtained from a Stern−Volmer analysis of $[HCO]_0$ that is formed from the photolysis of glyoxal, and the results from the two methods are consistent, providing further support for the occurrence of reaction R4.

To determine the quantum yield for HCO formation from glyoxal at wavelengths $\geq$395 nm, reaction R4 needs to be accounted for by recording the HCO time dependence following the photoexcitation laser pulse. If this is not performed and if a fixed nonzero delay is used to determine the HCO signal, then the assigned HCO quantum yield from glyoxal photolysis may be contaminated by reaction R4. This situation appears to be the case in the previous study by Zhu et al.[28] in which the HCO quantum yield was determined by monitoring the HCO at a fixed delay time of 15 μs with respect to the photoexcitation laser. However, in the presence of air, triplet glyoxal, $(HCO)_2(T_1)$, is expected to be rapidly quenched by oxygen, and hence reaction R4 is not expected to have any atmospheric implications.

Acknowledgment. This work was supported by an EPSRC grant GR/T28560/01 and the EU SCOUT program.

References and Notes

(1) Hatakeyama, S.; Washida, N.; Akimoto, H. *J. Phys. Chem.* **1986**, *90*, 173.

(2) Barnes, I.; Bastian, V.; Becker, K. H.; Overath, R.; Tong, Z. *Int. J. Chem. Kinet.* **1989**, *21*, 499.

(3) Yarwood, G.; Peng, N.; Niki, H. *J. Phys. Chem.* **1991**, *95*, 7330.

(4) Magneron, I.; Mellouki, A.; Le Bras, G.; Moortgat, G. K.; Horowitz, A.; Wirtz, K. J. *J. Phys. Chem. A* **2005**, *109*, 4552.

(5) Atkinson, R. *Atmos. Environ.* **2000**, *34*, 2063.
(6) Bandow, H.; Washida, N. *Bull. Chem. Soc. Jpn.* **1985**, *58*, 2549.
(7) Tuazon, E. C.; MacLeod, H.; Atkinson, R.; Carter, W. P. L. *Environ. Sci. Technol.* **1986**, *20*, 383.
(8) Kean, A. J.; Grosjean, E.; Grosjean, D.; Harley, R. A. *Environ. Sci. Technol.* **2001**, *35*, 4198.
(9) Grosjean, E.; Green, P. G.; Grosjean, D. *Analytic. Chem.* **1999**, *71*, 1851.
(10) Beirle, S.; Volkamer, R.; Wittrock, F.; Richter, A.; Burrows, J.; Platt, U.; Wagner, T. *Geophys. Res. Lett.* **2005**, *32*, L11810.
(11) Volkamer, R.; Spietz, P.; Burrows, J.; Platt, U. *J. Photochem. Photobiol., A* **2005**, *172*, 35.
(12) Feierabend, K. J.; Zhu, L.; Talukdar, R. K.; Burkholder, J. B. *J. Phys. Chem. A* **2008**, *112*, 73.
(13) Plum, C. N.; Sanhueza, E.; Atkinson, R.; Carter, W. P. L.; Pitts, J. N., Jr. *Environ. Sci. Technol.* **1983**, *17*, 479.
(14) Moortgat, G. K. *Pure Appl. Chem.* **2001**, *73*, 487.
(15) Colberg, M.; Friedrichs, G. *J. Phys. Chem. A* **2006**, *110*, 160.
(16) Nesbitt, F. L.; Gleason, J. F.; Stief, L. J. *J. Phys. Chem. A* **1999**, *103*, 3038.
(17) Jang, M.; Kamens, R. M. *Environ. Sci. Technol.* **2001**, *35*, 4758.
(18) Liggio, J.; Li, S.-M.; McLaren, R. *Environ. Sci. Technol.* **2005**, *39*, 1532.
(19) Hastings, W. P.; Koehler, C. A.; Bailey, E. L.; De Hann, D. O. *Environ. Sci. Technol.* **2005**, *39*, 8728.
(20) Anderson, L. G.; Parmenter, C. S.; Poland, H. M. *Chem. Phys.* **1973**, *1*, 401.
(21) Tadić, J.; Moortgat, G. K.; Wirtz, K. J. *J. Photochem. Photobiol., A* **2006**, *177*, 116.
(22) Loge, G. W.; Parmenter, C. S. *J. Phys. Chem.* **1981**, *85*, 1653.
(23) Dobeck, L. M.; Lambert, H. M.; Kong, W.; Pisano, P. J.; Houston, P. L. *J. Phys. Chem. A* **1999**, *103*, 10312.
(24) Burak, I.; Hepburn, J. W.; Sivkumar, N.; Hall, G. E.; Chawla, G.; Houston, P. L. *J. Chem. Phys.* **1987**, *86*, 1258.
(25) Hepburn, J. W.; Buss, R. J.; Butler, L. J.; Lee, Y. T. *J. Phys. Chem.* **1983**, *87*, 3638.
(26) Chen, M.-W.; Lee, S. J.; Chen, I.-C. *J. Chem. Phys.* **2003**, *119*, 8347.
(27) Kao, C. C.; Ho, M.; Chen, M.; Lee, S.; Chen, I. *J. Chem. Phys.* **2004**, *120*, 5087.
(28) Chen, Y.; Zhu, L. *J. Phys. Chem. A* **2003**, *107*, 4643.
(29) Langford, A. O.; Moore, C. B. *J. Chem. Phys.* **1984**, *80*, 4211.
(30) Calvert, J. G.; Layne, G. S. *J. Am. Chem. Soc.* **1953**, *75*, 856.
(31) Brown, S. S.; Ravishankara, A. R.; Stark, H. *J. Phys. Chem. A* **2000**, *104*, 7044.
(32) Baulch, D. L.; Cobos, C. J.; Cox, R. A.; Esser, C.; Frank, P.; Just, Th.; Kerr, J. A.; Pilling, M. J.; Troe, J.; Walker, R. W.; Warnatz, J. *J. Phys. Chem. Ref. Data* **1992**, *21*, 411.
(33) Salter, R. J.; Blitz, M. A.; Heard, D. E.; Kovacs, T.; Pilling, M. J.; Seakins, P. W. **2009**, manuscript in preparation.
(34) Huisman, A. J.; Hottle, J. R.; Coens, K. L.; DiGangi, J. P.; Galloway, M. M.; Kammrath, A.; Keutsch, F. N. *Anal. Chem.* **2008**, *80*, 5884.
(35) Blitz, M. A.; Heard, D. E.; Pilling, M. J. *J. Phys. Chem. A* **2006**, *110*, 6742.
(36) Curtis, A. R. *Biochem. Soc. Trans.* **1976**, *4*, 364.
(37) Burcat, A.; Ruscic, B. Ideal Gas Thermochemical Database with updates from Active Thermochemical Tables, http://garfield.chem.elte.hu/Burcat/burcat.html ed.
(38) Zhu, L.; Kellis, D.; Ding, C.-F. *Chem. Phys. Lett.* **1996**, *257*, 487.
(39) Flad, J. E.; Brown, S. S.; Burkholder, J. B.; Stark, H.; Ravishankara, A. R. *Phys. Chem. Chem. Phys.* **2006**, *8*, 3636.

JP9030249